Scale interactions of turbulence subjected to a straining–relaxation–destraining cycle

By JUN CHEN[1], CHARLES MENEVEAU[1,2] AND JOSEPH KATZ[1,2]

[1]Department of Mechanical Engineering, Johns Hopkins University, Baltimore, MD 21218, USA

[2]Centre of Environmental and Applied Fluid Mechanics, Johns Hopkins University, Baltimore, MD 21218, USA

The response of turbulence subjected to planar straining and de-straining is studied experimentally, and the impact of the applied distortions on the energy transfer across different length scales is quantified. The data are obtained using planar particle image velocimetry (PIV) in a water tank, in which high-Reynolds-number turbulence with very low mean velocity is generated by an array of spinning grids. Planar straining and de-straining mean flows are produced by pushing and pulling a rectangular piston towards, and away from, the bottom wall of the tank. The data are processed to yield the time evolution of Reynolds stresses, anisotropy tensors, turbulence kinetic energy production, and mean subgrid-scale (SGS) dissipation rate at various scales. During straining, the production rises rapidly. After the relaxation period the small-scale SGS stresses recover isotropy, but the Reynolds stresses still display significant anisotropy. Thus when destraining is applied, a strong negative production (mean backscatter) occurs, i.e. the turbulence returns kinetic energy to the mean flow. The SGS dissipation displays similar behaviour at large filter scales, but the mean backscatter gradually disappears with decreasing filter scales. Energy spectra are compared to predictions of rapid distortion theory (RDT). Good agreement is found for the initial response but, as expected for the time-scale ratios of the experiment, turbulence relaxation causes discrepancies between measurements and RDT at later times.

1. Introduction

Turbulent flows exhibit strong interaction between different scales, including momentum and kinetic energy exchange. At high Reynolds numbers, the range of the scales involved can span several decades. Better understanding of scale interactions is important for successful application of turbulence prediction methods, especially when the turbulence interacts with mean velocity gradients and is not in equilibrium conditions with the mean flow.

In the Reynolds-averaged Navier–Stokes (RANS) approach, the Reynolds stress tensor, $-\rho\langle u'_i u'_j\rangle$, must be appropriately modelled in order to close the equations. The energy exchange between mean flow and turbulence is accounted for in the transport equation of turbulent kinetic energy ($k \equiv (1/2)\langle u'_i u'_i\rangle$) (Tennekes & Lumley 1972; Pope 2000). There, the turbulence production rate

$$\Psi \equiv -\langle u'_i u'_j\rangle \frac{\partial \langle u_i\rangle}{\partial x_j} \tag{1.1}$$

quantifies the energy supply from the mean flow to the turbulence, and its typically positive value indicates flux of kinetic energy from the mean flow to the turbulence. The viscous dissipation rate term, $\varepsilon \equiv 2\nu\langle s_{ij}s_{ij}\rangle$, accounts for the energy drain by the viscous stresses, where $s_{ij} \equiv (\partial u_i'/\partial x_j + \partial u_j'/\partial x_i)/2$ is the fluctuating rate of strain tensor.

In large-eddy simulation (LES) (e.g. Rogallo & Moin 1984; Reynolds 1990; Pope 2000), a flow variable $f(\boldsymbol{x}, t)$ is filtered into a coarse-scale part

$$\widetilde{f}(\boldsymbol{x}, t) = \int_D f(\boldsymbol{x} - \boldsymbol{x}', t) G_{\Delta}(\boldsymbol{x}') \, \mathrm{d}\boldsymbol{x}' \qquad (1.2)$$

and a small-scale (or subgrid scale, SGS) part

$$f^{SG}(\boldsymbol{x}, t) = f(\boldsymbol{x}, t) - \widetilde{f}(\boldsymbol{x}, t), \qquad (1.3)$$

where $G_{\Delta}(\boldsymbol{x}')$ represents a filter kernel with characteristics scale Δ. Similar to the Reynolds stress in the RANS equations, the subgrid scale (SGS) stress, $\tau_{ij} = \widetilde{u_i u_j} - \widetilde{u}_i \widetilde{u}_j$, must be properly modelled in order to close the LES equations. The crucial influence of the SGS stress on the resolved flow field is accounted for in the transport equation of resolved kinetic energy, $k_{\Delta} \equiv \frac{1}{2}\widetilde{u}_i \widetilde{u}_i$ (Piomelli *et al.* 1991; Pope 2000). The term $-\tau_{ij}\widetilde{S}_{ij}$, commonly referred to as SGS dissipation, quantitatively describes the local energy transfer between resolved and subgrid scales. While on average the typical trend of energy transfer is from resolved to subgrid scales (forward scattering), locally in a turbulent flow, the subgrid scales often return energy to resolved scales (back scattering) (Piomelli *et al.* 1991; Liu, Meneveau & Katz 1994). The mean SGS dissipation,

$$\Pi_{\Delta} = -\langle\tau_{ij}\widetilde{S}_{ij}\rangle, \qquad (1.4)$$

is the net energy transfer across scale Δ.

In most engineering applications, turbulent flows are regularly subjected to strong large-scale mean deformation. Examples include turbulent flows inside contracting or expanding channels, flows inside pumps, ship hull boundary layers impinging on propeller blade, etc. Such deformations have the ability to affect significant ranges of turbulence scales and may thus affect quantities of interest in LES, such as the SGS dissipation and the performance of SGS models. When the turbulence-to-mean-flow time ratio is very large, i.e. $Sk/\varepsilon \to \infty$, where S characterizes the strength of the mean flow velocity gradients, rapid distortion theory (RDT) has been introduced as a means of simplifying the Navier–Stokes equations (Prandtl 1933; Taylor 1935; Batchelor & Proudman 1954; Savill 1987; Hunt & Carruthers 1990; Pope 2000). The resulting RDT equations are linear with respect to the fluctuating part, and thus can be solved analytically. Turbulent fields predicted by RDT depend on the total strain, $e(t) = \int_{t_0}^{t} S(t') \, \mathrm{d}t'$.

The interactions between turbulence and strong mean flow velocity gradients have been studied using both RANS and LES frameworks. In the context of the RANS, Townsend (1954), Keffer (1965) and Tucker & Reynolds (1968) conducted hot-wire measurements of decaying grid turbulence inside a specially designed distorting section of wind tunnel. One may also refer to the experiments reported in Gence & Mathieu (1979, 1980), Kevlahan & Hunt (1997) and Choi & Lumley (2001). Lee & Reynolds (1985) performed DNS of strained turbulence and explored different straining schemes, including planar and axisymmetric straining, at a microscale Reynolds number, R_{λ}, of less than 100. For turbulence subjected to mean shear, Saddoughi & Veeravalli (1994) performed high-resolution hot-wire measurements of

turbulent boundary layers in the world's largest wind tunnel, at $R_\lambda \sim 500 - 1500$ and $Sk/\varepsilon \sim 6-12$. In the context of LES, the PIV measurement by Liu, Katz & Meneveau (1999) provided insight on scale interactions and evolution of SGS statistics when a constant axisymmetric distortion ($Sk/\varepsilon \sim 7$) was applied on an initially isotropic turbulence. Among others, the results showed that the measured SGS stress anisotropy was smaller than the prediction of RDT and that eddy-viscosity type SGS models give biased predictions when strong straining was present. Their data ensemble was small (20 measurements at every time phase), creating significant scatter in the statistics and trends. To further elucidate the interaction of mean straining flow and turbulence, other types of applied straining, e.g. planar straining in the present study, must be studied with variations and combinations of straining histories.

Previous investigations of SGS physics predominantly focus on nearly equilibrium turbulence or equilibrium turbulence subjected to strong distortion (e.g. Liu *et al.* 1999; Meneveau & Katz 2000). A more complicated scenario exists when the turbulent flow is subjected to a sequence of straining and destraining. This process occurs, for instance, when turbulence impinges, and passes around, a propeller blade. Along the suction side, the free-stream turbulence is first compressed and then stretched by the mean flow, near the leading edge of the blade. In the middle section of a blade passage, the same turbulent fluid element is advected by nearly uniform mean flow (turbulence relaxation). Finally, the deformation is partially reversed (destraining) during passage in the pressure recovery part of the flow, near the trailing edge of the blade. This type of sequence also exists for turbulence below surface waves (Teixeira & Belcher 2002), and in internal combustion engines (Hadzic, Hanjalic & Laurence 2001). SGS physics and modelling in non-equilibrium conditions were studied also by Piomelli, Coleman & Kim (1997) in suddenly accelerated or sheared wall-layers.

In the present study, we investigate experimentally the evolution of turbulence subjected to a cycle of planar straining, relaxation and destraining from the perspective of both RANS and LES. The scale-interactions are documented as functions of length scale and time during the cycle. The main questions to be addressed are: (i) What is the relationship between RANS and LES variables, such as Reynolds and SGS stresses, as well as Reynolds production and SGS dissipation, as function of scale; (ii) How well does RDT predict the time evolution of the above mentioned parameters at different scales, when the strength of the applied straining is 'moderate', i.e. the $Sk/\varepsilon \to \infty$ validity criterion for RDT does not apply.

Details about the experimental apparatus and instrumentation are given in § 2. The characteristics of both initial turbulence and mean flow history are documented in § 3. Results and discussion are presented in § 4. Conclusions are drawn in § 5.

2. Experimental set-up

2.1. *Apparatus*

The experimental set-up is shown in figures 1 and 2. The same set-up has been used to study the performance of a series of sub-grid stress models, as described in Chen, Katz & Meneveau (2005). Since the facility and procedures are essential for interpreting the results, we provide a brief description also in this paper.

The facility is composed of a water tank, a turbulence generation mechanism, a straining system, and support frames. The dimensions of the water tank are $325(L) \times 125(H) \times 20(W) \, \mathrm{cm}^3$, with the test section located at the centre of the bottom portion of the tank. Windows below and on both sides of the test section provide
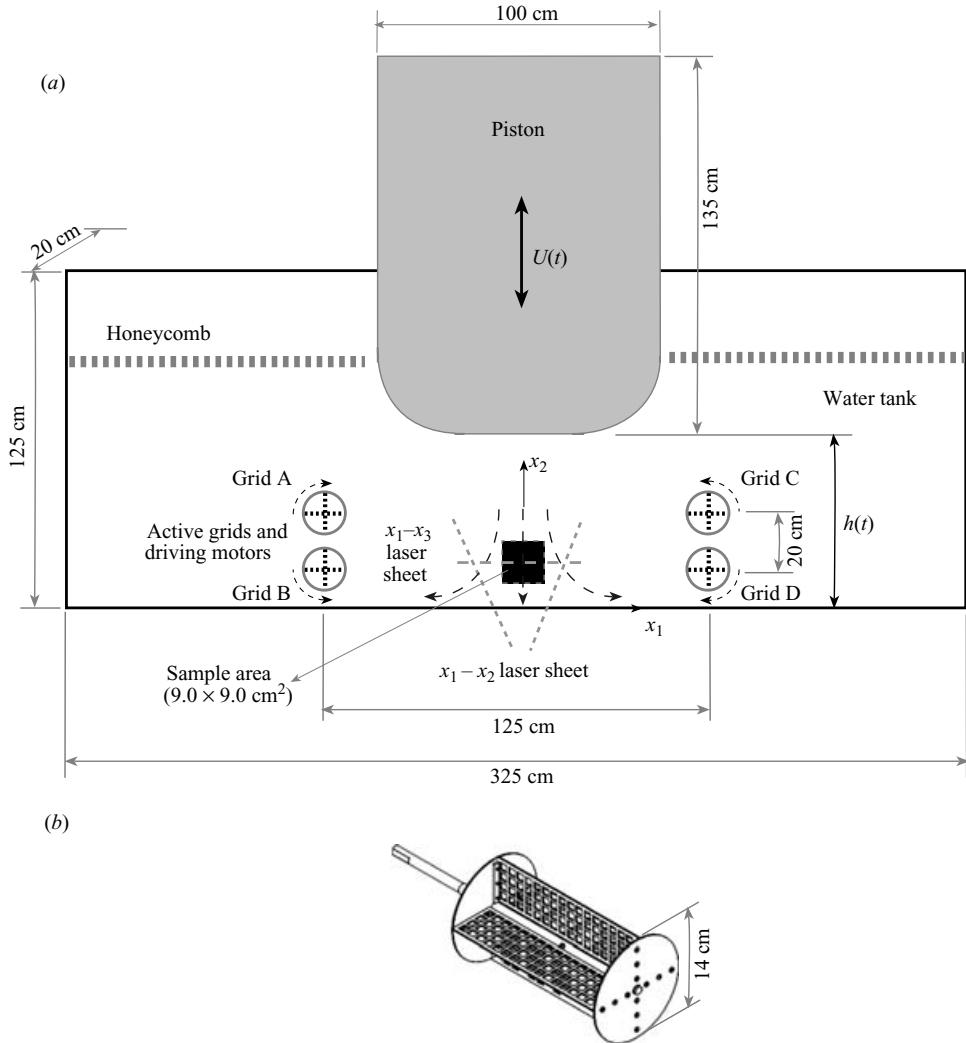
FIGURE 1. Schematic description of (a) the experimental facility, and (b) the active grids.

optical access for data acquisition. Two honeycomb plates are set at the top part of the water tank to alleviate the possible effects of surface waves.

In recent years, active grids have proved useful in generating high-Reynolds-number isotropic turbulence. For example, Makita (1991) devised a system of randomly flapping agitator wings inside a small wind tunnel, and obtained nearly homogenous and isotropic turbulence with $R_\lambda \sim 400$. Mydlarski & Warhaft (1996) employed the same idea to study the characteristics of turbulence at different Reynolds numbers ranging from 50 to 473, and the design was scaled up to reach $R_\lambda \sim 730$ (Mydlarski & Warhaft 1998; Kang, Chester & Meneveau 2003). See also Hwang & Eaton (2004) who used synthetic jet actuators. Liu *et al.* (1999) introduced four symmetrically deployed rotating grids to obtain isotropic turbulence with $R_\lambda \sim 290$ and weak mean flow. As in Liu *et al.* (1999) and Friedman & Katz (2002), in the present study, four rotating active grids are installed on both sides of the test section, as shown in figure 1. Each grid has four perforated metal blades with a solidity of 40%. The
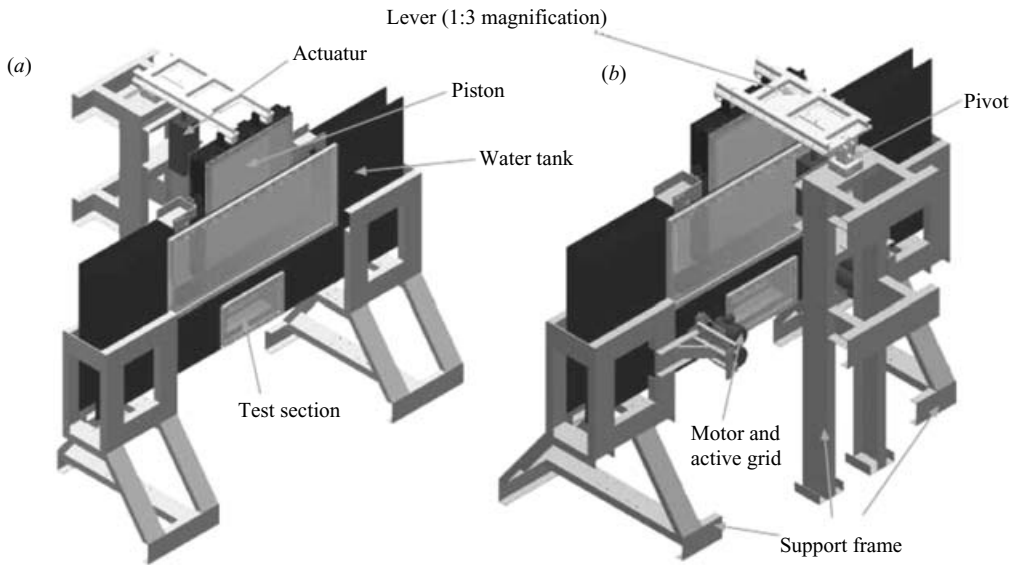
FIGURE 2. Perspective views of the facility showing the actuator and lever attached to the piston, the grid drivers, and the location of test section. (*a*) Front view; (*b*) back view.

location of the active grids has been decided based on prior experience (Liu *et al.* 1999; Friedman & Katz 2002) and by solving a one-dimensional diffusion equation using the $k-\epsilon$ equations with standard coefficients. The objectives are to place the grids as far as possible from the sample area (to avoid contaminating the latter with fluid passing through the grids and then being advected into the sample section during the destraining) while maximizing the turbulence intensity. An initial guess for the distance is determined by solving a one-dimensional diffusion problem using the $k-\epsilon$ equations. With the chosen distance, pure turbulent diffusion of k in the horizontal direction between the two grid pairs yields the desired level of k in the sample area. Half-horsepower a.c. motors are used to drive each grid, using variable frequency inverters (ABB, ACS 140) to provide independent speed control for each motor. The active grids can operate at constant speed independent of the load up to 500 r.p.m. The speed and rotation direction of each grid are adjusted separately in order to obtain optimal, most isotropic and homogeneous, turbulence characteristics. To acquire the data used in the present study, motors A and C run at 375 r.p.m., whereas motors B and D run at 450 r.p.m. The rotation orientation is shown in figure 1. The difference in motor speeds is required to offset the influence of the bottom tank wall on turbulence generation.

The response of turbulence subjected to irrotational straining has been investigated in wind tunnels for some time (e.g. Townsend 1954; Reynolds 1962; Keffer 1965; Tucker & Reynolds 1968; Gence & Mathieu 1979, 1980; Kopp, Kawall & Keffer 1995). In these studies, the straining has been generated by using a specially designed test section of varying cross-section. This approach has certain inherent drawbacks: (i) the turbulence is decaying along the flow passage, so the effect of the distortion is coupled with the inherent decay process, (ii) the boundary layers developing in the distorting section may influence the response of the turbulence, and (iii) the hot-wire technique gives valid information on structure only when the Taylor's hypothesis holds. Liu *et al.* (1999) explored techniques to overcome these drawbacks. In their experiments,

a pair of disks (15 cm diameter) were driven by a cam mechanism towards each other in a small water tank, generating irrotational axisymmetric straining between them. This straining is applied on the turbulence generated by the aforementioned active grids. This concept is extended in the present study to generate plane straining and destraining by translating a piston vertically inside the water tank, as shown in figures 1 and 2. For a piston height $h(t)$, the flow pattern induced underneath the piston bottom surface can be idealized by a two-dimensional stagnation-point flow. In the Cartesian coordinate system shown in figure 1, the strain rate tensor is given by

$$\mathbf{S}(t) = S(t) \begin{bmatrix} 1 & 0 & 0 \\ 0 & -1 & 0 \\ 0 & 0 & 0 \end{bmatrix}, \tag{2.1}$$

where $S(t) = -\dot{h}(t)/h(t)$ is the strain rate magnitude. If the piston moves towards the tank bottom, i.e. $S(t) > 0$, the process is referred to as 'straining'; if the piston moves away from the bottom, i.e. $S(t) < 0$, it is referred to as 'destraining' (reverse straining).

The dimensions of the piston are $100(L) \times 135(H) \times 18(W)\,\mathrm{cm}^3$ and it occupies almost the entire width of the tank. Its bottom surface has rounded corners to prevent flow separation. The piston is driven by a motion control system through a motion magnification lever with a ratio of 3:1, as shown in figure 2. The maximum displacement of the piston is 76.2 cm. The motion control system consists of an Exlar GS60-1010 linear electric actuator, an Emerson MX-1600 brushless drive, and an Emerson AXIMA2000 programmable motion control module, all illustrated in figure 3. The trajectory of the piston is programmed through the motion control module, enabling adjustment of the relevant parameters to obtain a desired trajectory. The piston trajectory designed for the present study is shown in figure 4. In each cycle, the piston moves downward to generate the straining, rests for a certain time (relaxation), and then moves upward to generate destraining. The trajectory of the piston is monitored by a high-speed video camera (Kodak Ektapro EM) operating at 250 frames per second. Results confirm that the motion control system is of good repeatability, with a position variance of 2 mm between different runs.

2.2. Instrumentation

Particle image velocimetry (PIV) is used to measure the velocity field. The light source is a dual-head Nd-YAG pulse laser (532 nm, 120 mJ), and the beam is expanded to a sheet, along the (x_1, x_2)-plane using spherical and cylindrical lenses. The flow field is uniformly seeded with hollow glass beads with spherical shape, median diameter 8–12 μm, and specific gravity 1.05–1.15. A Kodak ES-4.0 CCD camera, with 2048×2048 pixels resolution, is used to record the PIV images. The camera is operated under double-exposure mode, and records 5 image pairs per second. The time interval between the double exposures is $\Delta T = 2.0\,\mathrm{ms}$. In order to increase the temporal resolution of the statistics, four PIV measurement sequences are recorded at varying initial delays of 0.210, 0.260, 0.310 and 0.360 s, respectively. In this way, the measurements are performed at a temporal resolution of 50 ms.

As shown in figure 3, the motion control, the piston trajectory calibration, the laser control, and the PIV data acquisition are synchronized in order to obtain repeatable measurements at exactly the same timing in every cycle. At every temporal phase, the measurement is repeated 1000 times, which provides a good ensemble set for statistical analysis and convergence.

The PIV images are acquired into a computer through an XCAP image-grabbing hardware/software combination, and then undergo cross-correlation analysis using
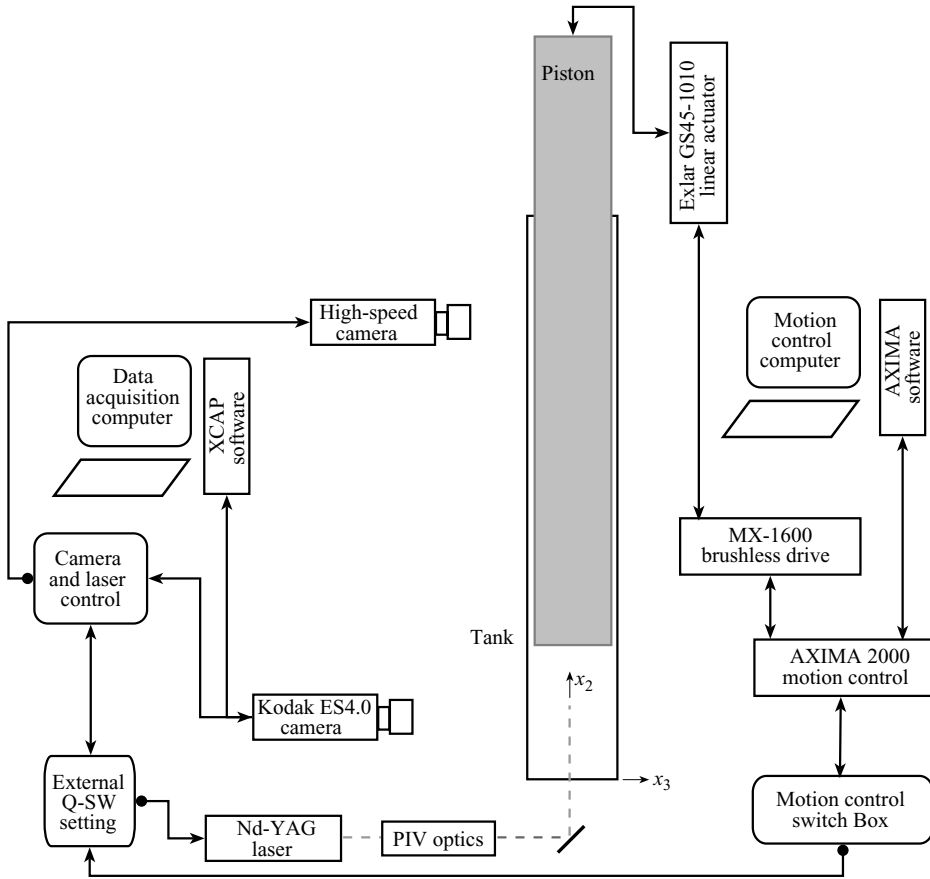
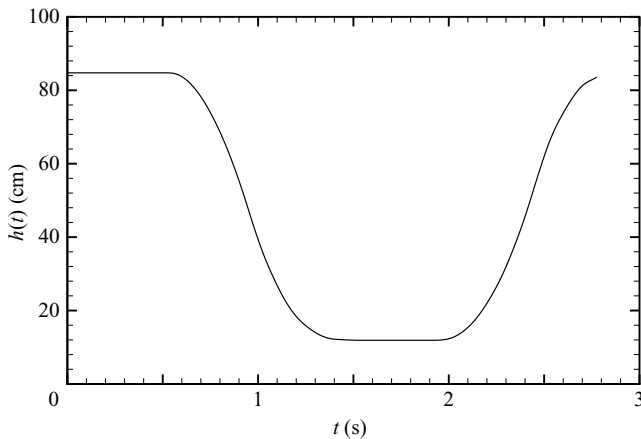FIGURE 3. Schematic diagram of the instrumentation and control system.

FIGURE 4. Piston motion trajectory.

in-house developed software, described in Roth, Mascenik & Katz (1999) and Roth & Katz (2001). The interrogation windows are 32×32 pixels, and the vector spacing is $\delta = 0.70$ mm (16 pixels, with 50% overlap). A total of 121×121 vectors are obtained from each image pair. The sample area is $9.0 \times 9.0\,\text{cm}^2$, of which the upper

$9.0 \times 7.5 \, \text{cm}^2$ is used during the analysis of turbulence behaviour. The lower $1.5 \, \text{cm}$ strip shows some bottom effect and thus is discarded. The centre of this sample area is located at $x_2 = 6.0 \, \text{cm}$.

The typical conservative uncertainty estimate of the instantaneous data from PIV measurement is 0.15 pixels, and the relative uncertainty is about 1.5% (for characteristic displacements of 10.0 pixels). Consequently, the uncertainties in variables involving mean velocity are about 0.06%, and those involving the r.m.s. values are about 0.4%. The uncertainty in terms involving mean velocity gradients is about 0.5%. Further details on errors and uncertainties in the present analysis procedure are presented in Roth & Katz (2001). Extended discussion on uncertainties in PIV analysis can be found, for example, in Keane & Adrian (1990), Huang, Diabiri & Gharib (1997) and Raffel, Willert & Kompenhans (1998).

Moreover, to quantify the characteristics of initial turbulence along the x_3 direction, in a separate set of experiments, a laser sheet illuminates the centreplane ($x_2 = 6.0 \, \text{cm}$) of the test section along the $x_1 - x_3$ direction, as shown in figure 1, where a $6 \, \text{cm} \times 6 \, \text{cm}$ sample area is recorded through a camera–mirror combination (perpendicular to that shown in figure 3). The same PIV recording hardware and analysis software are applied as described before. The initial turbulence measurements (without piston movement) are repeated 1000 times to accumulate statistics. 121×121 vectors are extracted from every instantaneous measurement, with a vector spacing of $0.45 \, \text{mm}$.

3. Flow characterization

To verify that the mean flow is two-dimensional, PIV measurements are conducted at several (x_1, x_2)-planes, i.e. at different x_3. These tests confirm that the mean flow keeps nearly the same two-dimensional distribution along the x_3-direction, except for areas near the sidewalls. The area of wall effects is limited to $3.5 \, \text{cm}$ away from the sidewalls. The data presented in this paper are obtained in the central plane ($x_3 = 0$). The characteristics of the mean flow pattern and turbulence are determined by statistical analysis of the ensemble set at the same piston phase.

In evaluating derivatives using finite differencing, two different kinds of grid, coarse and fine (figure 5), are used. Unless specially stated, the Reynolds averaged parameters are obtained using a fine grid δ, the PIV spatial resolution. For calculating the LES parameters associated with the resolved field such as filtered strain rate tensor $\widetilde{S}_{ij}$, we use a coarse grid Δ, the filter size. The derivatives on the fine grid are evaluated using a least-squares filter (Raffel *et al.* 1998; Foucaut & Stanislas 2002), e.g. at a discrete point indexed by (n, m)

$$\left\langle \frac{\partial u_i}{\partial x_j} \right\rangle \bigg|_{(n,m)} = \left\langle \frac{-2u_i|_{(n,m-2)} - u_i|_{(n,m-1)} + u_i|_{(n,m+1)} + 2u_i|_{(n,m+2)}}{10\delta} \right\rangle . \qquad (3.1)$$

This expression is obtained from a least-squares-error fit through 5 points on the PIV (fine) grid. As shown in Raffel *et al.* (1998) and Foucaut & Stanislas (2002), this method has proved effective for reducing the error of derivative calculations from PIV data. The coarse grid derivatives for LES variables are evaluated using central second-order derivative:

$$\frac{\partial \widetilde{u}_i}{\partial x_j} \bigg|_{(n',m')} = \frac{-\widetilde{u}_i|_{(n',m'-1)} + \widetilde{u}_i|_{(n',m'+1)}}{2\Delta} , \qquad (3.2)$$
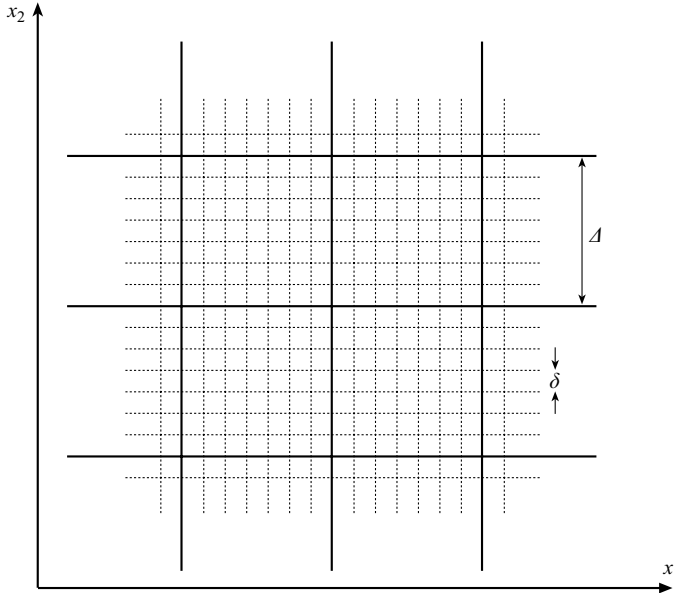
FIGURE 5. The fine grid (spacing $= \delta$) and coarse grid (spacing $= \Delta$).

where (n', m') are the nodes on the coarse grid. At this scale, the data are already very smooth and accurate derivatives can be evaluated from the two-point evaluation and there is no need for the 5-point least-squares method used on the fine grid.

3.1. *Initial turbulence*

The mean and root-mean-square fluctuation of the initial equilibrium turbulence before straining, $\langle u_i \rangle$ and u_i', are computed at every point $(x_1, x_2, x_3 = 0.0 \, \text{cm})$ and $(x_1, x_2 = 6.0 \, \text{cm}, x_3)$ and based on the data ensemble at $t = 0.210 \, \text{s}$. The spatially averaged mean velocity components in all three directions are significantly smaller than the mean velocities applied by the straining and destraining (given later). The spatial distributions of r.m.s. values of velocity fluctuations, shown in figure 6, reflect good spatial homogeneity for $x_2 > 0.03 \, \text{m}$. Only data in this nearly homogeneous region are used in the analysis hereinafter. The r.m.s values of velocity, spatially averaged over the 9 cm $\times$ 7.5 cm sample area, are given in table 1. They significantly exceed the magnitudes of mean flow. The degree of anisotropy is around 1.1, which is close to the anisotropy obtained in traditional grid turbulence (valued between 1.0 and 1.1), and less than the values of active grid turbulence, of about 1.2 (Makita 1991; Mydlarski & Warhaft 1996; Kang *et al.* 2003). The one-dimensional kinetic energy spectra of the initial homogenous turbulence are calculated, and shown in figure 7.

These spectra are calculated using data along four lines near the central area (κ_i follows the direction of x_i). The ensemble mean velocity of every point is subtracted, and the data are linearly detrended before fast Fourier transform (FFT) is applied to calculate the spectra. The result is then averaged over the four lines, and over the 1000 realizations in the ensemble set. The solid line reproduces the Kolmogorov $-5/3$ spectrum for the inertial range (Tennekes & Lumley 1972; Hinze 1987):

$$E_{11}(\kappa_1) = \tfrac{18}{55} C_\kappa \varepsilon^{2/3} \kappa_1^{-5/3} \qquad (3.3)$$

where C_k is the Kolmogorov constant, taken as $C_\kappa = 1.7$ in the present study. Comparing the longitudinal and transverse spectra provides a criterion to check
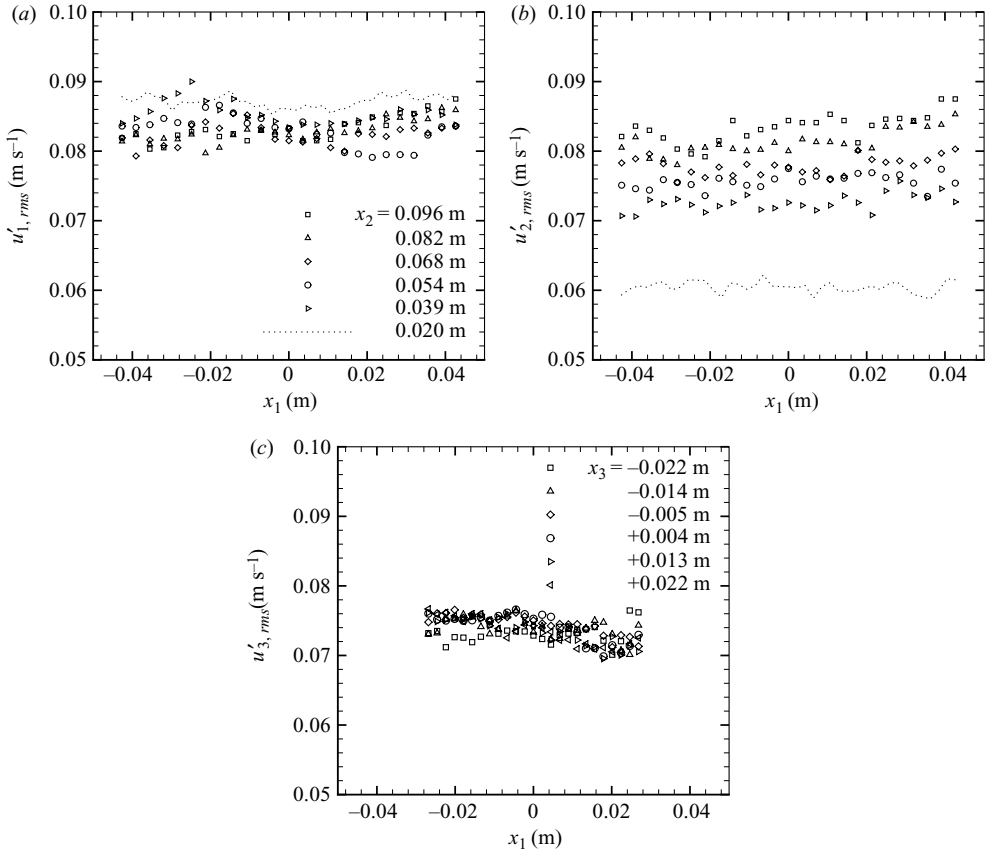
FIGURE 6. Root mean square values of velocity fluctuations at $t = 0.210$ s: (*a*) $u'_{1,rms}(\mathbf{x}, t)$ at different x_2 layers, (*b*) $u'_{2,rms}(\mathbf{x}, t)$ at different x_2 layers with the same legend as (*a*), and (*c*) $u'_{3,rms}(\mathbf{x}, t)$ at different x_3 layers. For clarity, only one fifth of the values are plotted. Lines in (*a*) and (*b*) give the typical values in the lower 1.5 cm strip in (x_1, x_2)-plane measurements which are influenced by bottom effect and thus discarded in analysis.

the local isotropy of the turbulence (e.g. Elsner & Elsner 1996). The six curves show fairly good agreement, except for the high-wavenumber range, which verifies that the initial equilibrium turbulence is nearly isotropic (Monin & Yaglom 1971). The slight 'tail-up' near the highest wavenumber in the spectra is caused by the PIV measurement noise (Liu *et al.* 1994; Eggles *et al.* 1994). The homogeneity of the flow at different scales is also verified by comparing energy spectra at different locations (not shown). For such a nearly homogeneous isotropic turbulent flow, the dissipation rate of the initial turbulence, ε_0, can be estimated by curve-fitting equation (3.3) to the measured spectra in the inertial range. Doron *et al.* (2001) gives a comparison of several methods used to estimate ε from PIV data. The estimated dissipation rate and other parameters of the initial turbulence are given table 1. The initial Kolmogorov scale η_0 is smaller than the resolution of the present experiment ($\delta \approx 5\eta_0$). The Taylor-scale Reynolds number based on the initial state of turbulence is $R_\lambda \sim 400$, higher than the value reported in Liu *et al.* (1999).

    The estimated integral scale ($l_0 \sim 13$ cm) is larger than the size of sample area (9 cm). Therefore, turbulence length-scales larger than the sample area cannot be resolved

Mean velocity	$\langle u_1 \rangle$	$-0.003\,\mathrm{m\,s^{-1}}$
	$\langle u_2 \rangle$	$0.029\,\mathrm{m\,s^{-1}}$
	$\langle u_3 \rangle$	$-0.004\,\mathrm{m\,s^{-1}}$
Root mean square value of velocity fluctuations	$\langle u'_{1,rms} \rangle$	$0.084\,\mathrm{m\,s^{-1}}$
	$\langle u'_{2,rms} \rangle$	$0.076\,\mathrm{m\,s^{-1}}$
	$\langle u'_{3,rms} \rangle$	$0.074\,\mathrm{m\,s^{-1}}$
Degree of anisotropy ($x_1 - x_2$ plane)	$\langle u'_{1,rms} \rangle / \langle u'_{2,rms} \rangle$	1.11
Degree of anisotropy ($x_1 - x_3$ plane)	$\langle u'_{1,rms} \rangle / \langle u'_{3,rms} \rangle$	1.13
Characteristic turbulence velocity	$u' = \dfrac{\langle u'_{1,rms} \rangle + \langle u'_{2,rms} \rangle + \langle u'_{3,rms} \rangle}{3}$	$0.078\,\mathrm{m\,s^{-1}}$
Turbulence kinetic energy	$k_0 = \frac{3}{2}u'^2$	$0.0092\,\mathrm{m^2\,s^{-2}}$
Turbulence dissipation rate (from $E_{11}(\kappa_1)$)	ε_0	$0.0035\,\mathrm{m^2\,s^3}$
Integral scale	$l_0 \sim u'^3 / \varepsilon_0$	$0.13\,\mathrm{m}$
Taylor's microscale	$\lambda_0 \sim u'\sqrt{15\nu/\varepsilon_0}$	$0.0050\,\mathrm{m}$
Kolmogorov length scale	$\eta_0 \sim (\nu^3/\varepsilon_0)^{1/4}$	$140\,\mathrm{\mu m}$
Microscale Reynolds number	$R_\lambda \equiv u'\lambda_0/\nu$	400

TABLE 1. Flow parameters of the initial equilibrium turbulence ($t = 0.210\,\mathrm{s}$), where values in the x_3 direction are from (x_1, x_3)-plane measurements.
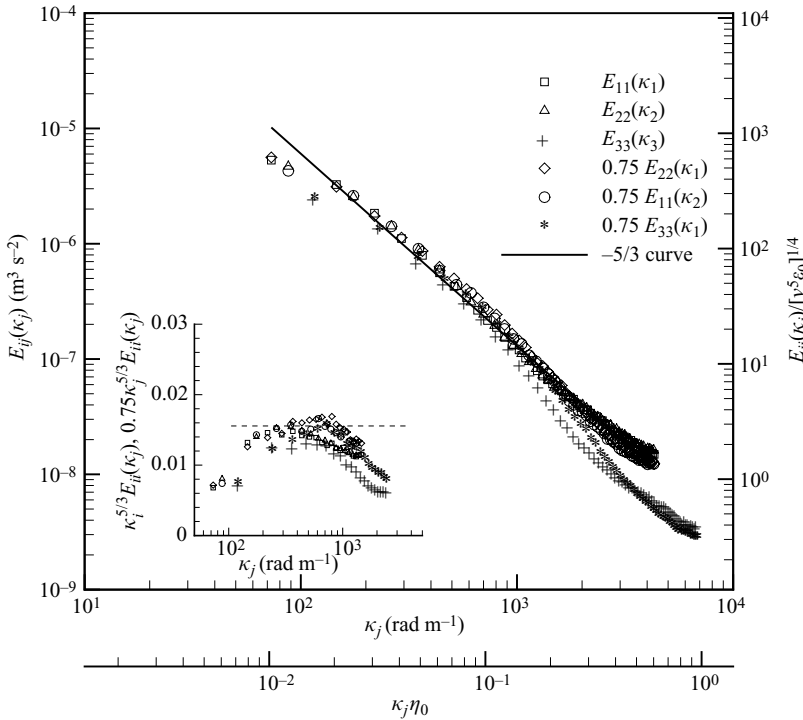

FIGURE 7. One-dimensional kinetic energy spectra of the initial equilibrium turbulence ($t = 0.210\,\mathrm{s}$). Inset: pre-multiplied spectra $\kappa_i^{5/3} E_{ii}(\kappa_i)$ and $\kappa_j^{5/3} \frac{3}{4} E_{ii}(\kappa_j)$ (no summation over repeated indices here).

directly using the present data. However, their contribution to velocity variance is accounted for using time averaging over the 1000 data sets.
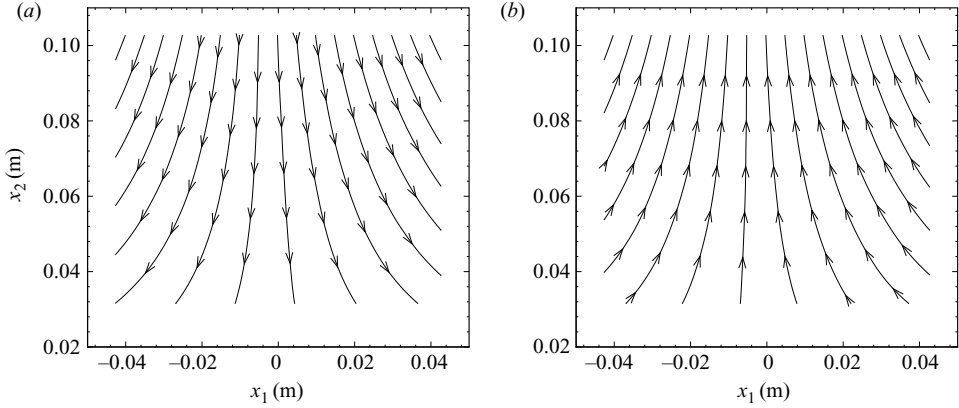
FIGURE 8. Mean flow streamline patterns at (*a*) $t = 1.160$ s, and (*b*) $t = 2.160$ s.
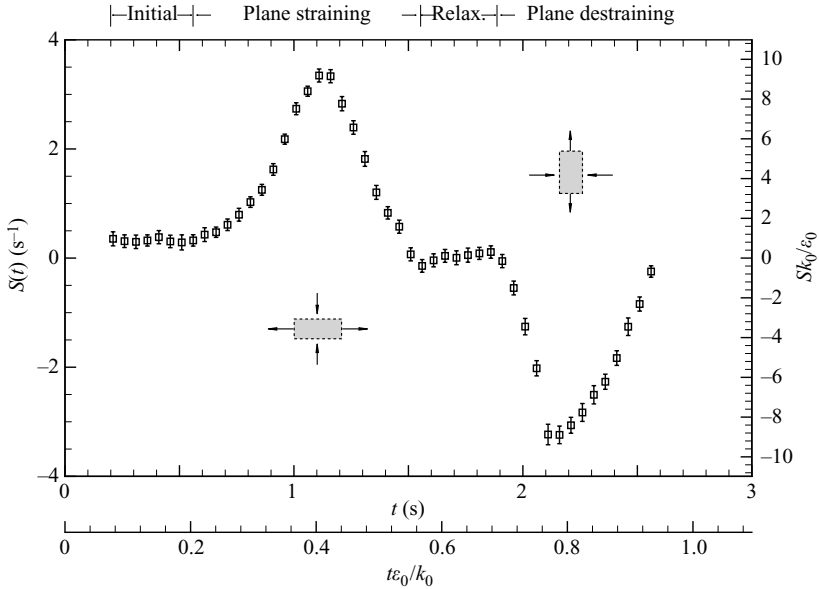

FIGURE 9. Evolution of mean strain rate, $S(t)$. The error bars represent the standard deviation across the spatial distribution in the sample area.

3.2. *Mean flow*

Figures 8(*a*) and 8(*b*) show some streamlines of the ensemble-averaged flow, illustrating the stagnation-point-type mean flow patterns during time phases with strong straining and destraining, respectively. The strain rate tensor of the mean flow is evaluated using $S_{11}(\boldsymbol{x}, t) = \partial \langle u_1(\boldsymbol{x}, t) \rangle / \partial x_1$, $S_{22}(\boldsymbol{x}, t) = \partial \langle u_2(\boldsymbol{x}, t) \rangle / \partial x_2$, and the characteristic strain rate is $S \equiv (S_{11} - S_{22})/2$. The time evolution of the spatially averaged value of S is given in figure 9. The magnitudes of S_{11} and S_{22} are very close to each other during the entire cycle, with $S_{11} = -S_{22}$, as shown in figure 5 of Chen *et al.* (2005). The small deviations from the spatially averaged value confirm that the applied straining and destraining are nearly uniform across the sample area. According to the sign of mean strain rate, the cycle can be divided into four regimes: initial equilibrium: plane straining; relaxation; and plane destraining. The magnitudes
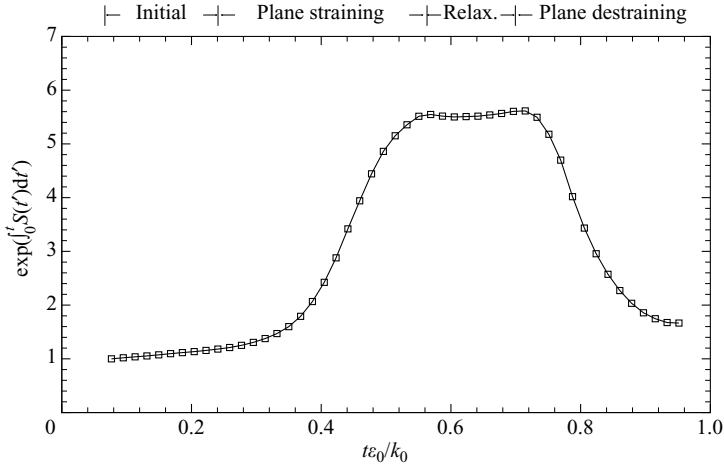
FIGURE 10. Evolution of total deformation.

of peak straining and destraining are both about $3.5\,\mathrm{s}^{-1}$. The maximum turbulence-to-mean-strain time ratio is $S_{max}k_0/\varepsilon_0 \sim 9.5$. The evolution of total distortion, $e(t)$, defined in §1 and calculated by using trapezoidal integration, is shown in figure 10. The total deformation reaches nearly 6, i.e. an initially square fluid parcel is deformed into a thin horizontal rectangle, which is six times as long as its initial size. Also, the deformation is nearly reversed by the end of the cycle.

4. Results

4.1. *Evolution of Reynolds stresses and turbulence production*

After calculating the turbulent velocity variances (or the negative of the kinematic Reynolds stress), $\langle u_i' u_j' \rangle$, at every point, we determine their spatial mean and r.m.s. values over the sample area. The temporal evolution of the spatial mean of $\langle u_i' u_j' \rangle$ is presented in figure 11. Because of the two-dimensional nature of the present planar PIV, only $\langle u_1' u_1' \rangle$, $\langle u_2' u_2' \rangle$, and $\langle u_1' u_2' \rangle$ are obtained (in future experiments, it would be of interest to measure the response of the velocity variances in the third direction). During the entire cycle, all three terms display good spatial homogeneity, as reflected from the narrow standard deviation, except near the end, after $t \sim 2.4\,\mathrm{s}$. The shear term is virtually zero everywhere, in accord with expectation when the principal axes of applied strain rate align with x_1 and x_2. During the first half of the straining phase, with increasing strain magnitude, $\langle u_1' u_1' \rangle$ decreases while $\langle u_2' u_2' \rangle$ increases, i.e. the principal axes of the Reynolds stress tensor are aligned with those of the straining when the initial turbulence is isotropic (Gence & Mathieu 1979, 1980). Both terms reach their peak/trough values around $t\varepsilon_0/k_0 \sim 0.5$, which indicates a clear delay with respect to the timing of peak straining $t\varepsilon_0/k_0 \sim 0.4$. After that, until the end of the relaxation regime, $\langle u_2' u_2' \rangle$ decreases gradually and $\langle u_1' u_1' \rangle$ stays approximately constant. At the end of the relaxation regime, $\langle u_1' u_1' \rangle$ and $\langle u_2' u_2' \rangle$ still differ from each other, showing that the turbulence has not yet returned to a fully isotropic state. When the straining is absent, the turbulent velocity variance evolves towards its original isotropic state, but does not reach it. During the destraining regime, $\langle u_1' u_1' \rangle$ responds promptly to the applied destraining and increases from its previous plateau value, while $\langle u_2' u_2' \rangle$ continues the trend of decreasing, reaching a minimum value later
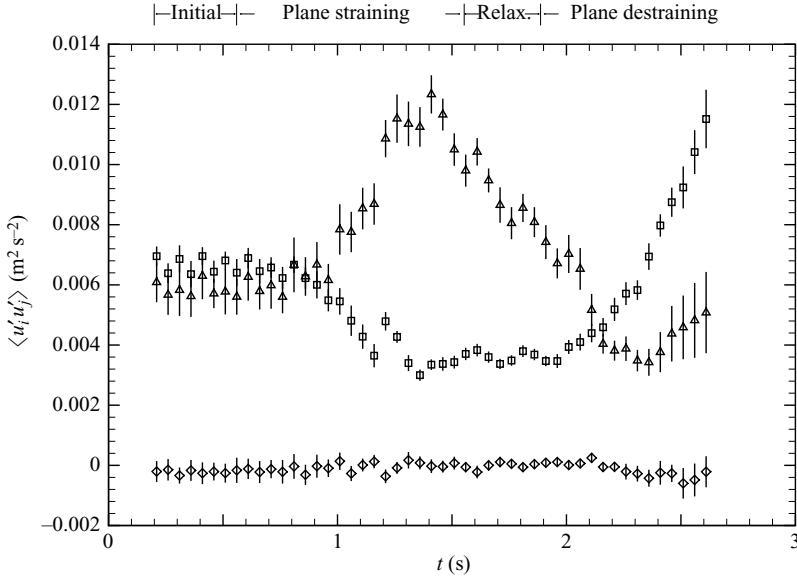
FIGURE 11. Evolution of turbulent velocity variance $\langle u_i' u_j' \rangle$. The error bars represent the standard deviation of the spatial distribution in the sample area. Squares $\langle u_1' u_1' \rangle$; triangles, $\langle u_2' u_2' \rangle$; diamonds, $\langle u_1' u_2' \rangle$.

than the peak destraining. The values of $\langle u_1' u_1' \rangle$ increase during the entire destraining phase. Since the principal axes of the applied destraining are perpendicular to those of the straining phase, the Reynolds stress tensor seems to adjust itself under the influence of destraining, first by returning to the isotropic state, and then by aligning with the principal axes of the destraining.

The homogeneity of turbulence during the whole cycle is further investigated by comparing the spatial average of the variances in four equal-sized subsets of the sample area. The subsets are four horizontal rectangles A, B, C and D, as shown in figure 12. During the entire straining and destraining cycle, the turbulence remains reasonably homogeneous. Only at $t > 2.5$ s are there systematic differences visible for $\langle u_2' u_2' \rangle$.

To compare the present data with RDT prediction, we evaluate the normalized Reynolds stresses, r_{ij}, defined as

$$r_{ij} = \frac{\langle u_j' u_j' \rangle}{\langle u_j' u_j' \rangle_{t_0}}, \tag{4.1}$$

where the subscript t_0 denotes the initial value at $t = 0.210$ s. The standard anisotropy tensor

$$b_{ij} = \frac{r_{ij}}{r_{ll}} - \tfrac{1}{3} \delta_{ij} \qquad (i, j = 1, 2, 3) \tag{4.2}$$

is replaced in the present study by a two-dimensional surrogate to avoid making assumptions about the missing out-of-plane components, i.e.

$$b_{ij} = \frac{r_{ij}}{r_{11} + r_{22}} - \tfrac{1}{2} \delta_{ij} \qquad (i, j = 1, 2). \tag{4.3}$$

The results are shown in figures 13 and 14, together with the prediction of RDT. The RDT calculations used in the present study are described in Appendix A.
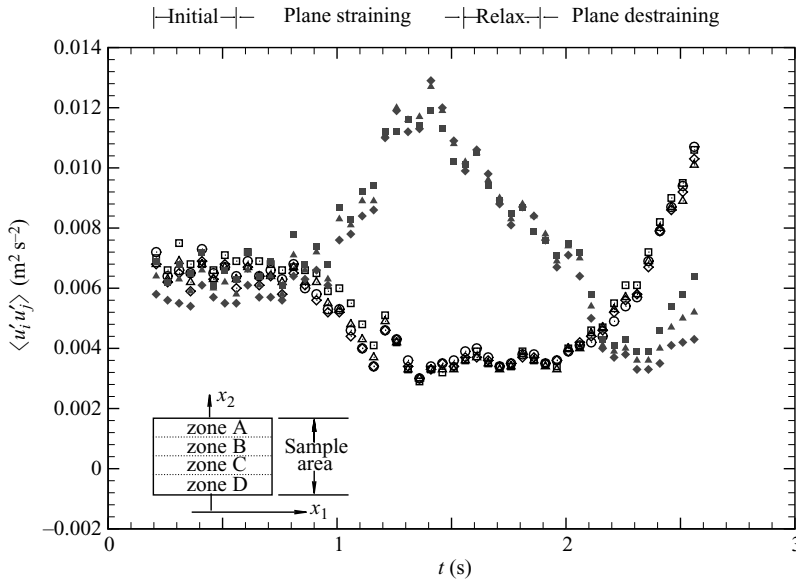
FIGURE 12. Evolution of turbulent velocity variance $\langle u_1' u_1' \rangle$ (open symbols) and $\langle u_2' u_2' \rangle$ (filled symbols) at different horizontal zones. Squares, zone A; triangles, zone B; diamonds, zone C; circles, zone D.
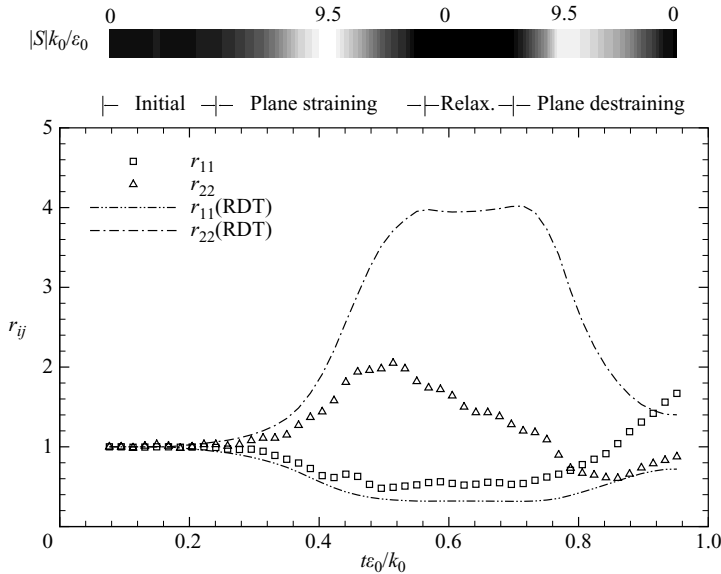

FIGURE 13. Evolution of normalized Reynolds stress and the prediction of RDT (r_{ij}, equation (4.1)). The top contour bar shows the strength of the applied straining.

RDT gives the correct trend of the response of r_{11} and r_{22} when straining is applied, but overestimates r_{22} and underestimates r_{11}, thus over-predicting the degree of anisotropy. The peak of r_{22} predicted by RDT appears later than that obtained from the measurements. As the relaxation starts, the measured b_{22} (note that $b_{11} = -b_{22}$) begins to decrease, i.e. it returns to an isotropic state slowly, but does not reach isotropy
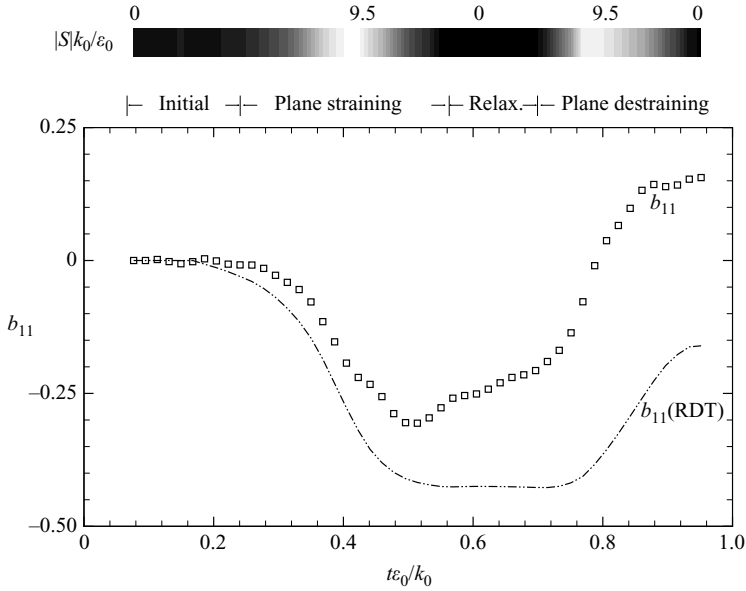
FIGURE 14. Evolution of the two-dimensional surrogate of the anisotropy tensor (equation (4.3)), and prediction of RDT. Note that $b_{22} = -b_{11}$.
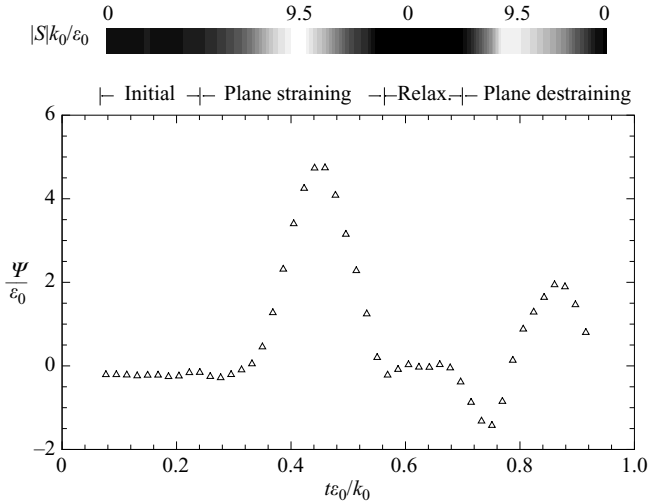

FIGURE 15. Evolution of turbulence production $\Psi = -\langle u_1' u_1' \rangle S_{11} - \langle u_2' u_2' \rangle S_{22}$.

at the end of the relaxation phase (incomplete relaxation). When the destraining is applied, the rapid response forces the Reynolds stresses back to isotropy first, and then continuously to anisotropy, this time with $b_{11} > b_{22}$. In summary, RDT qualitatively predicts the correct trends of the response of Reynolds stresses, but the magnitudes are comparable to the experimental data only at initial times.

The evolution of energy exchange between mean flow and turbulence, Ψ, as defined in equation (1.1), is shown in figure 15. We can only calculate the in-plane components, but since the mean flow is two-dimensional, the production rate is approximated very

well from the in-plane components. During the straining period, Ψ follows the amplitude of applied strain, which reveals that straining causes energy exchange from mean flow to turbulence, as expected. Once the straining stops, Ψ goes to zero since $\partial \langle u_i \rangle / \partial x_j \sim 0$. During the destraining period, Ψ first goes to a negative value, returns to zero, and then reaches a positive peak, which is much smaller than the peak value during the straining phase. Detailed examination of the data verifies that the strong negative value of Ψ at the beginning of destraining phase is not caused by spatial non-homogeneity or measurement uncertainty. Such a global backscattering, i.e. turbulent structures returning energy back to the mean flow, is also observed by Gence & Mathieu (1979) in their wind-tunnel experiments, when a second distortion is applied immediately after the first one, and the principal axes of the two distortions are perpendicular. Using $\langle S_{11} \rangle = -\langle S_{22} \rangle$, the production can be written as $\Psi = (\langle u_2' u_2' \rangle - \langle u_1' u_1' \rangle) S(t)$. Thus, a negative Ψ occurs when destraining ($S(t) < 0$) is applied on anisotropic turbulence with $\langle u_1' u_1' \rangle < \langle u_2' u_2' \rangle$, and Ψ returns to zero when the turbulence crosses through the isotropic state. Note that RDT predicts a strong negative Ψ during the destraining phase, whose peak amplitude ($\Psi/\varepsilon_0|_{max} = -16.0$) is comparable with that during straining (not shown).

4.2. *Evolution of SGS stresses and SGS dissipation*

Using equation (1.2), a two-dimensional top-hat filter with scale Δ, i.e. a filter kernel

$$G_\Delta(x_1, x_2) = \begin{cases} 1/\Delta^2 & \text{if } |x_1| < \Delta/2, \quad |x_2| < \Delta/2, \\ 0 & \text{otherwise,} \end{cases} \qquad (4.4)$$

is applied on the velocity field in order to investigate scale-interactions of turbulence in an LES framework. Figure 16 shows the evolution of $\langle \tau_{11} \rangle$ and $\langle \tau_{22} \rangle$, the ensemble-averaged sub-grid stresses, for three filter scales, $\Delta = 25\eta_0$, $\Delta = 50\eta_0$ and $\Delta = 100\eta_0$. As expected, the mean SGS shear stress, $\langle \tau_{12} \rangle$, is virtually zero everywhere (not shown). For homogenous turbulence, $\langle \tau_{ii} \rangle / (\varepsilon_0 \Delta)^{2/3}$ (no summation in i) should be scale-independent if Δ is within the inertial range (Liu *et al.* 1999; Pope 2000). During the whole cycle, the present $\Delta = 25\eta_0$ curve clearly falls below the other two, because $\Delta = 25\eta_0$ already approaches the viscous dissipation range. Conversely, the $\Delta = 50\eta_0$ and $\Delta = 100\eta_0$ curves are close to each other, but are not equal, over the entire cycle.

Similar to equation (4.3), the two-dimensional surrogate of the anisotropy tensor of mean SGS stresses is defined here as:

$$b_{ij}^\tau \equiv \frac{r_{ij}^\tau}{r_{11}^\tau + r_{22}^\tau} - \tfrac{1}{2}\delta_{ij}, \qquad (4.5)$$

where r_{ij}^τ is the stress normalized by its initial value:

$$r_{ij}^\tau \equiv \frac{\langle \tau_{ij} \rangle}{\langle \tau_{ij} \rangle_{t_0}}. \qquad (4.6)$$

As is evident from figure 17, the anisotropy increases with filter scale, and its evolution during the cycle follows the evolution of mean strain, which is different from the evolution of the Reynolds stress anisotropy tensor, shown in figure 14. During the straining period, b_{11}^τ follows the evolution of the applied strain at all three filter scales. At the starting point of the relaxation period, although $\langle \tau_{11} \rangle$ and $\langle \tau_{22} \rangle$ do not return to the initial state (figure 16), b_{11}^τ shows isotropy from this time on, lasting until the end of the relaxation period. During the destraining period, b_{22}^τ decreases in a manner that is similar to that of b_{11}^τ during the straining period; but the behaviour of $\langle \tau_{11} \rangle$ during the destraining period does not even qualitatively resemble the behaviour of
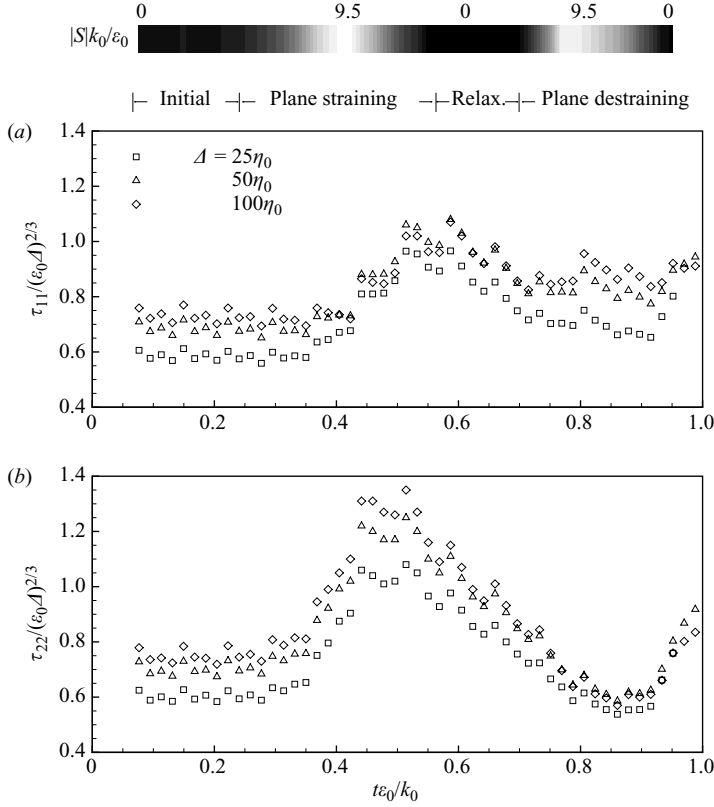
FIGURE 16. Evolution of normalized SGS stresses with three different filter scales.
(a) $\langle \tau_{11} \rangle / (\varepsilon_0 \Delta)^{2/3}$ and (b) $\langle \tau_{22} \rangle / (\varepsilon_0 \Delta)^{2/3}$.
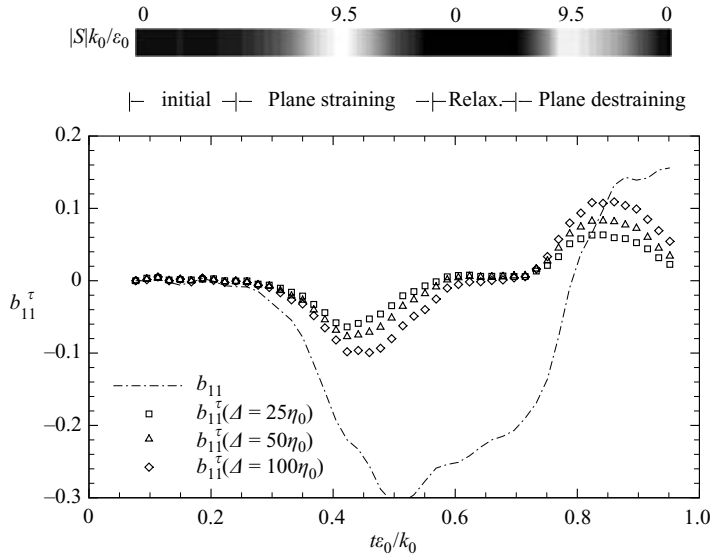

FIGURE 17. Evolution of b_{11}^τ with three different filter scales. Note that $b_{22}^\tau = -b_{11}^\tau$. For comparison, b_{11} is also plotted.

$\langle \tau_{22} \rangle$ during straining. Both $\langle \tau_{11} \rangle$ and $\langle \tau_{22} \rangle$ exhibit a delayed response to the applied straining.

Following Liu *et al.* (1999), the measured instantaneous velocity is decomposed into turbulent and mean parts due to the applied straining:

$$u_i(\boldsymbol{x}, t) = u_i^T(\boldsymbol{x}, t) + u_i^M(\boldsymbol{x}, t), \tag{4.7}$$

where the mean part is given by

$$u_i^M(\boldsymbol{x}, t) = (-1)^{i+1} S(t)\big(x_i - x_i^0\big), \tag{4.8}$$

and (x_1^0, x_2^0) is the location of stagnation point. Thus, the SGS stresses can be separated into three parts: turbulent; cross-term; and the applied straining parts:

$$\tau_{ij}(\boldsymbol{x}, t) = \tau_{ij}^T(\boldsymbol{x}, t) + \tau_{ij}^C(\boldsymbol{x}, t) + \tau_{ij}^M(\boldsymbol{x}, t). \tag{4.9}$$

The turbulent part is:

$$\tau_{ij}^T(\boldsymbol{x}, t) = \widetilde{u_i^T u_j^T} - \widetilde{u}_i^T \widetilde{u}_j^T. \tag{4.10}$$

The cross-term, representing the interaction between turbulence and applied straining, is:

$$\tau_{ij}^C(\boldsymbol{x}, t) = \big(\widetilde{u_i^T u_j^M} - \widetilde{u}_i^T \widetilde{u}_j^M\big) + \big(\widetilde{u_j^T u_i^M} - \widetilde{u}_j^T \widetilde{u}_i^M\big), \tag{4.11}$$

and the SGS stress generated by the applied straining is:

$$\tau_{ij}^M(\boldsymbol{x}, t) = \widetilde{u_i^M u_j^M} - \widetilde{u}_i^M \widetilde{u}_j^M. \tag{4.12}$$

Liu *et al.* (1999) investigated the dependence of $\langle \tau_{ij}^T \rangle$, $\langle \tau_{ij}^M \rangle$, and $\langle \tau_{ij}^C \rangle$ on Δ, and concluded that when the filter scale is small, the mean turbulence part, $\langle \tau_{ij}^T \rangle$, dominates the total SGS stress. In the following discussion, we examine the effect of each term on the SGS dissipation.

A two-dimensional surrogate of the SGS dissipation, Π_Δ (equation (1.4)), is evaluated based on the available data, i.e.

$$\Pi_\Delta^{2D} = -(\langle \tau_{11} \widetilde{S}_{11} \rangle + \langle \tau_{22} \widetilde{S}_{22} \rangle + 2\langle \tau_{12} \widetilde{S}_{12} \rangle). \tag{4.13}$$

Its evolution at three filter scales is presented in figure 18. Prior to straining, the SGS dissipation is nearly scale-independent, as expected in the inertial range. However, during straining, the SGS dissipation significantly increases with filter scale, owing to the non-equilibrium condition. Then, during the relaxation regime, all three curves nearly collapse, suggesting a scale-independent behaviour under the unforced relaxation conditions. The most salient feature of this plot is that the dissipation peak in the destraining period is significantly lower than the peak in the straining period, although the amplitudes of the straining and destraining are about the same. Furthermore, the SGS dissipation has a minimum during the destraining phase, which is lower even than the initial values. These apparent inconsistencies may be related to the reverse energy transfer mechanism discussed in §4.1. From figure 19, the contributions of τ_{ij}^T, τ_{ij}^M, and τ_{ij}^C to the SGS dissipation are clearly depicted: τ_{ij}^T is the dominant one, and the two mean terms ($-\langle \tau_{11}^M \widetilde{S}_{11} \rangle$ and $-\langle \tau_{22}^M \widetilde{S}_{22} \rangle$) cancel each other's contribution to the total SGS dissipation.

4.3. *Transition between subgrid and Reynolds-averaged variables*

This section focuses specifically on how the SGS variables tend to the RANS variables as Δ increases towards the integral scale, l_0. To perform this analysis, the SGS stress is calculated over a wide range of filter scales, from $25\eta_0$ up to $430\eta_0$. At the largest filter
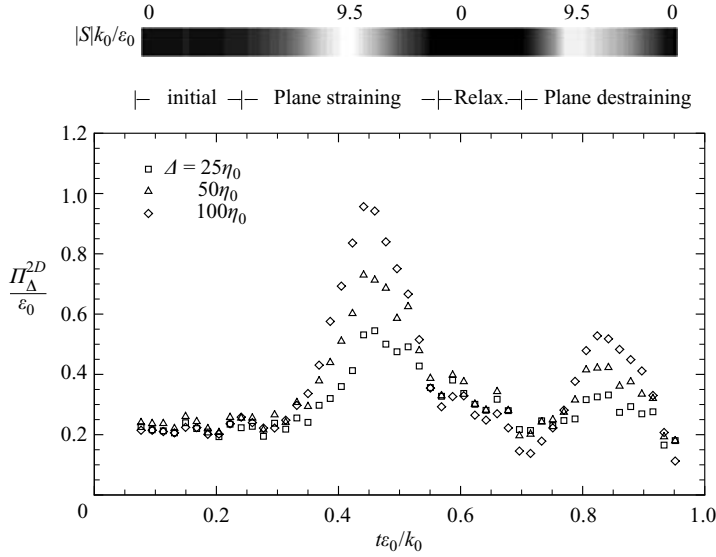
FIGURE 18. Evolution of Π_{Δ}^{2D} at three different filter scales.
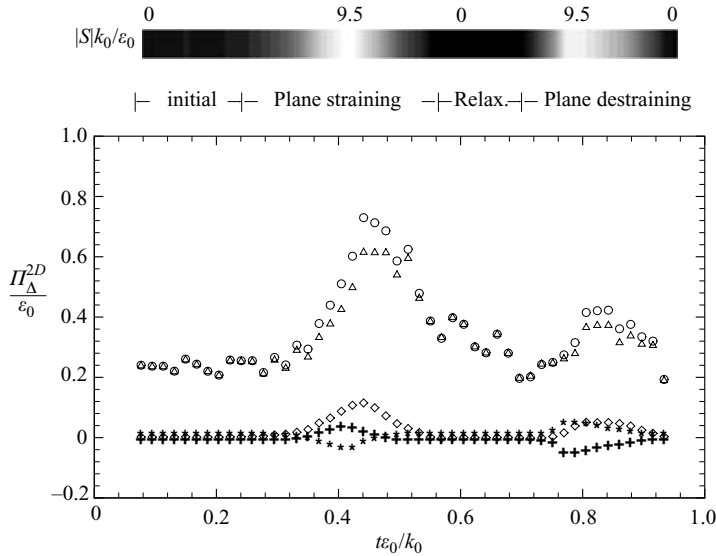
FIGURE 19. Evolution of different parts of Π_{Δ}^{2D} for $\Delta = 50\eta_0$. Circle, Π_{Δ}^{2D} ($-\langle \tau_{ij} \widetilde{S}_{ij} \rangle$); diamonds, $-\langle \tau_{ij}^C \widetilde{S}_{ij} \rangle$; triangles, $-\langle \tau_{ij}^T \widetilde{S}_{ij} \rangle$; asterisks, $-\langle \tau_{11}^M \widetilde{S}_{11} \rangle$; crosses, $-\langle \tau_{22}^M \widetilde{S}_{22} \rangle$.

scale of $\Delta_{max} = 430\eta_0 = 0.06$ m, strips of width $\Delta_{max}/2 = 0.03$ m must be excluded from the analysis. For consistency at all scales, the analysis is thus restricted to a rectangle with $x_1 \in (-0.012\,\text{m}, 0.012\,\text{m})$ and $x_2 \in (0.062\,\text{m}, 0.072\,\text{m})$ so that the convolutions that require data at $x_1 \pm \Delta/2$ are well defined for all Δ considered. Figure 20 shows the evolution of b_{11}^τ at different scales. The response lag of b_{11}^τ to the applied straining and destraining varies with filter scale. The small scales respond faster than the large scales, which indicates a mechanism more consistent with RDT than the 'energy
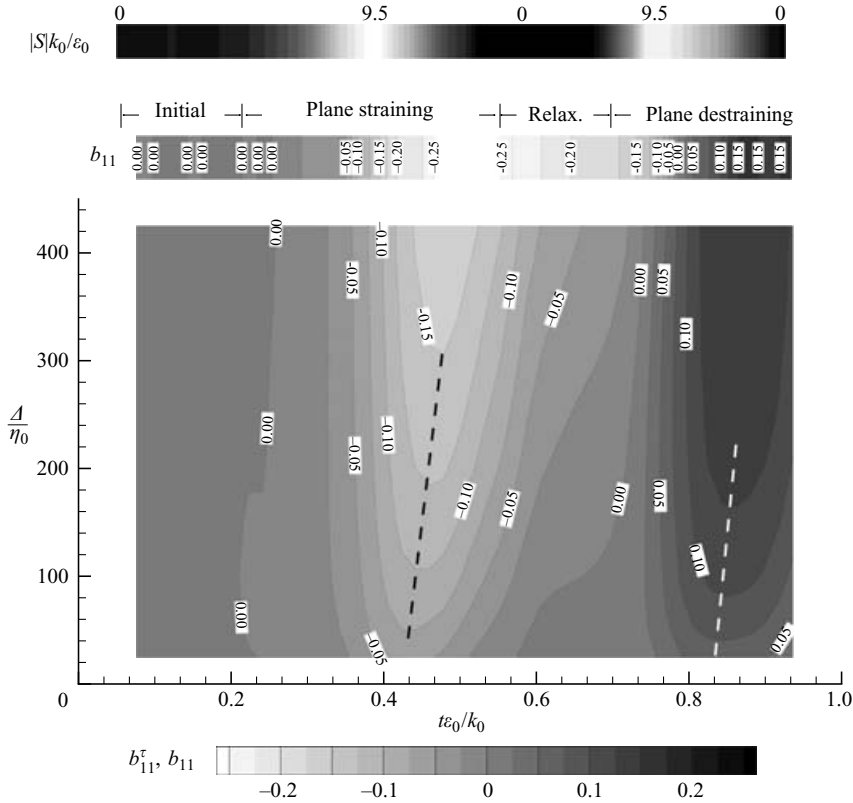
FIGURE 20. Evolution of SGS stress anisotropy (b_{11}^τ, bottom contour) at different filter scales as well as the Reynolds stress anisotropy (b_{11}, middle contour). Dash lines connect the peak values of b_{11}^τ during straining and destraining periods.

cascade' process in which the energy is first fed into the large scales before it cascades to small scales.

When the LES filter scale Δ is large enough in a spatially homogeneous flow, namely, when Δ approaches the integral scale, the resolved velocity $\widetilde{u}_i$ approaches the mean velocity $\langle u_i \rangle$, and the SGS part, $u_i - \widetilde{u}_i$, tends to the fluctuating velocity u_i'. As a consequence, the SGS stress τ_{ij} tends to the Reynolds stress $\langle u_i' u_j' \rangle$ (e.g. Pope 2000), as verified in figure 20 both in trends of magnitude and in the delayed response. Note that in our present data, $l_0/\eta_0 \sim 928$.

Next, a similar scale-dependent analysis is performed for Π_Δ^{2D} as a function of Δ. Because of the finite size of the resolved velocity field, it is not possible to compute $\widetilde{S}_{ij}$ at the regular coarse grid (see figure 5) when $\Delta > 33\delta$ ($\Delta > 165\eta_0$). Thus, to obtain Π_Δ^{2D} at larger filter scales, the velocity derivatives are evaluated on a semi-coarse grid ($\Delta' = 5\delta$). The results are shown in figure 21. As Δ approaches l_0, the trends of the mean SGS dissipation clearly tend toward the turbulence production. Overall, Π_Δ^{2D} is smaller in magnitude than Ψ because several terms are not included. In isotropic turbulence, we can show that $\Pi_\Delta^{2D} = 7/15 \Pi_\Delta^{3D}$, thus it is expected that Π_Δ^{2D} is a significant underestimate of the real SGS dissipation. The peak value of $\Psi/\varepsilon_0 (\sim 5)$ and the peak value of $\Pi_\Delta/\varepsilon_0 (\sim 3)$ are consistent with this ratio. Another possible contribution to the difference is the fact that our largest Δ is still smaller than the integral scale.
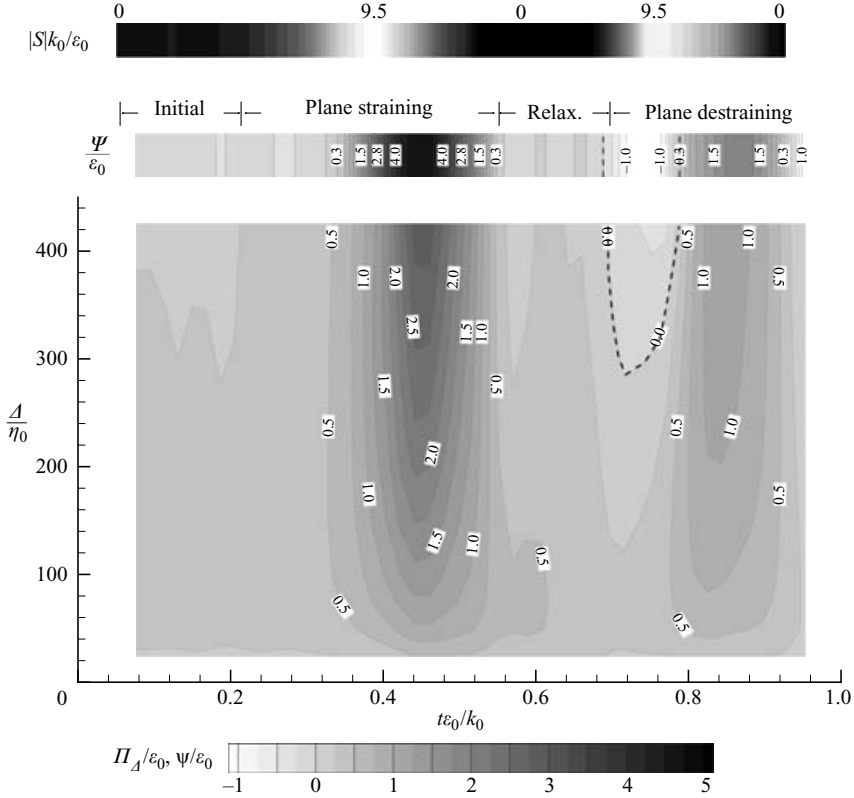
FIGURE 21. Evolution of two-dimensional surrogate mean SGS dissipation at different filter scales (Π_Δ^{2D}, bottom contour) and the turbulence production (Ψ, middle contour). Dashed lines enclose the back-scattering region at the beginning of the destraining period.

Global SGS back-scatter ($\Pi_\Delta < 0$) occurs at the beginning of the destraining phase when the filter scale is large enough, at about $\Delta = 300\eta_0 \sim l_0/3$. The magnitude and timing of the negative peak converges to that of the negative production ($\Psi < 0$, RANS back-scattering) as Δ increases. Such global back-scattering presents a challenge for most SGS models, especially the eddy-viscosity type models, which inherently cannot model negative production. This problem applies also to dynamic and scale-dependent dynamic Smagorinsky models. Owing to such a reversal in energy transfer at large scale, the SGS dissipation at small scales during the destraining period is also much lower than that during the straining period.

4.4. *Evolution of energy spectra and RDT predictions*

The homogeneity of turbulence during the entire cycle enables detailed investigation of energy at different scales by examining the evolution of one-dimensional energy spectra. Figure 22 presents the evolution of $E_{11}(\kappa_1)$ and $E_{22}(\kappa_1)$, and the corresponding RDT predictions by using a model spectrum (see Appendix A). Figure 23 shows the details of the evolution for three characteristic values of κ_1, corresponding to low (case A), middle (case B), and high (case C) inertial range wavenumbers, respectively. The case B curves represent the scale where the time scale of the turbulence is comparable to that of the applied straining, i.e. $(\Delta_s^2/\varepsilon_0)^{1/3} \sim 1/S$, namely $\Delta_s = \sqrt{\varepsilon_0/S^3} \sim 9$ mm. In case A, the turbulence turnover time is larger than that
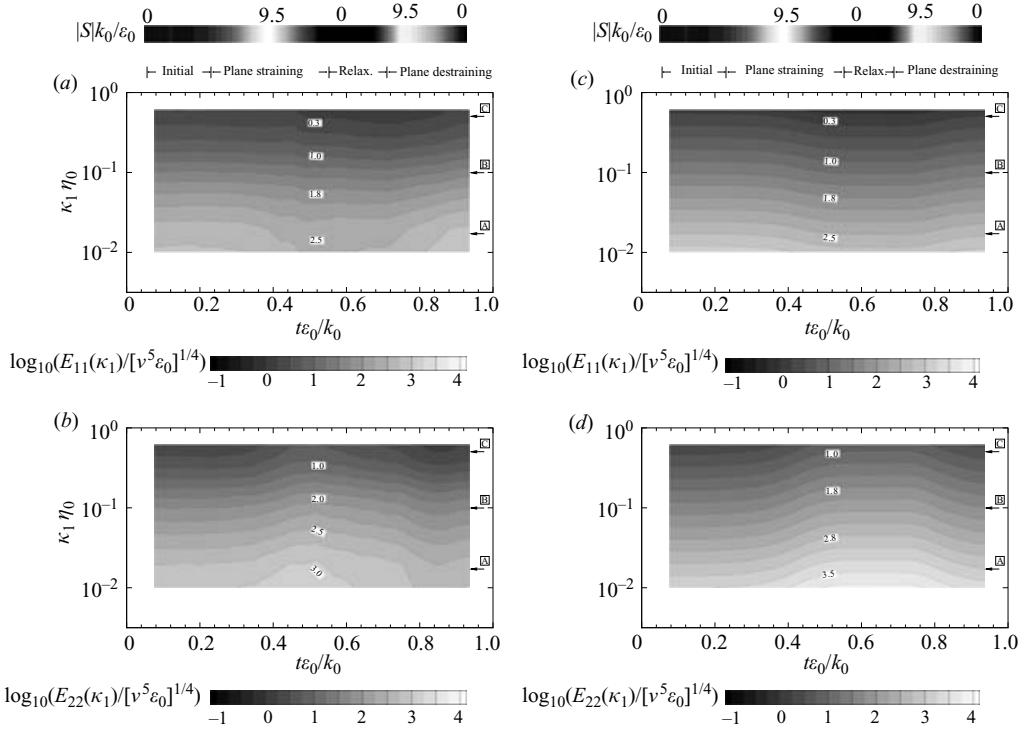
FIGURE 22. Evolution of the experimental: (*a*) $E_{11}(\kappa_1)$ and (*b*) $E_{22}(\kappa_1)$, and prediction of RDT: (*c*) $E_{11}(\kappa_1)$ and (*d*) $E_{22}(\kappa_1)$. For reference to figure 23: case A, $\kappa_1\eta_0 = 0.02$; case B, $\kappa_1\eta_0 = 0.10$; case C, $\kappa_1\eta_0 = 0.50$.

of the applied straining, i.e. more consistent with the RDT requirements, and in case C, $(\Delta_s^2/\varepsilon_0)^{1/3} < 1/S$.

RDT gives relatively good predictions of $E_{11}(\kappa_1)$, especially at large scales, during the straining and relaxation regimes. During the destraining phase, the prediction at small scales is better. As the relaxation starts, $E_{11}(\kappa_1)$ at large scales maintains nearly constant values since there is no mean strain to produce additional turbulence, while the small-scale structures are still active, dissipating energy. Thus, during this period RDT captures the evolution of energy at large scales more accurately than at small scales. During the initial stage of destraining, where back-scattering exists (figure 21), $E_{11}(\kappa_1)$ grows at all resolved scales.

RDT predicts the correct increase of $E_{22}(\kappa_1)$ until the first half of the straining process. After that point, RDT gives an excessively large prediction of $E_{22}(\kappa_1)$ at all scales. $E_{22}(\kappa_1)$ starts decreasing at the end of the straining phase. The 'forced' decrease of $E_{22}(\kappa_1)$ during the back-scattering phase is manifested here by a faster decay rate than the 'free' decay during the relaxation phase. $E_{22}(\kappa_1)$ increases slightly during the second half of destraining.

5. Summary and conclusions

This experimental study examines the response of turbulence to a cycle consisting of planar straining, relaxation and planar destraining. The experimental facility enables us to produce flows with the following characteristics. (*a*) Initial conditions consisting
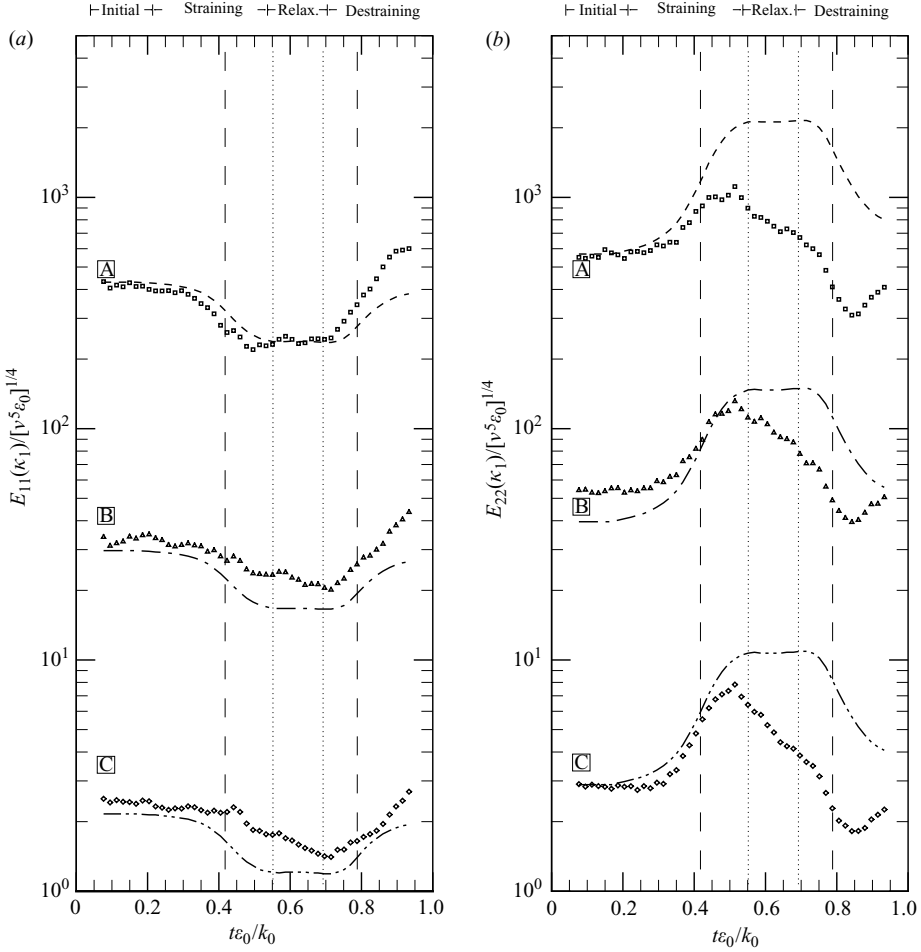
FIGURE 23. Evolution of one-dimensional power spectra at different wavenumbers (symbols) and the corresponding RDT prediction (lines). (a) $E_{11}(\kappa_1)$ and (b) $E_{22}(\kappa_1)$. Vertical dashed lines mark the timings of straining and destraining peaks, while the vertical dotted lines mark the start and end of the relaxation period, respectively. Case A, $\kappa_1\eta_0 = 0.02$; case B, $\kappa_1\eta_0 = 0.10$; case C, $\kappa_1\eta_0 = 0.50$.

of a high turbulence level with weak mean flow. (b) The initial turbulence follows the Kolmogorov $-5/3$ spectrum in most of the measured range of wavenumbers, with good local isotropy. (c) The initial turbulent Reynolds number is relatively high, $R_\lambda \sim 400$. (d) A moving piston creates two-dimensional stagnation-point flow in the sample area with near spatially uniform strain rate. (e) The maximum characteristic turbulence-to-mean-strain time scale ratio is $S_{max}k_0/\varepsilon_0 \sim 9.5$.

Data are obtained using planar PIV and the response of turbulence is studied in both RANS and LES frameworks. The data are compared with RDT predictions in both frameworks during the entire applied straining cycle. The following observations are made.

(a) The turbulence displays good spatial homogeneity during almost the complete straining–relaxation–destraining process, as confirmed by comparing the response of Reynolds stresses at different sections of the sample area.

(*b*) Once the straining is applied on the initially isotropic turbulence, as expected from RDT, $\langle u_1' u_1' \rangle$, the stress in the extended direction, decreases and $\langle u_2' u_2' \rangle$, the compressed component, increases. The principal axes of the Reynolds stress remain aligned with those of the applied straining. During the relaxation regime, the Reynolds stress starts recovering towards the original isotropic state, but does not reach it when the destraining is applied (incomplete relaxation). The destraining first forces the Reynolds stresses back to an isotropic state, and then aligns the principal axes of the Reynolds stress with those of the destraining, i.e. $\langle u_2' u_2' \rangle$ decreases and $\langle u_1' u_1' \rangle$ increases. RDT predicts the correct trend of Reynolds stresses until the straining peak, but deviates from the experimental results after that point owing to turbulence relaxation.

(*c*) When the destraining is applied on the anisotropic turbulence remaining after the incomplete relaxation, global negative production occurs, implying that turbulence loses energy to the mean flow (back-scatter). This negative production is caused by a mismatch between the orientation of straining and the magnitude of Reynolds stresses generated by prior processes.

(*d*) The SGS stresses approach the trends of Reynolds stresses as the filter scale increases. The lag in response of the SGS stresses to the applied straining increases as Δ increases. This lag causes several problems in application of scale-dependent dynamic models, as described in Chen *et al.* (2005). At large scales, the SGS dissipation is negative (back-scatter) during the initial stage of destraining, and approaches that of turbulence production at large scales. This global energy back-scattering would be a challenge to all eddy-viscosity type SGS models.

(*e*) RDT gives correct overall predictions of one-dimensional spectra only until the peak straining. Subsequent deviations are due to relaxation, expected to occur for turbulence at the time scales prevalent in the present experiment.

(*f*) The data obtained in the present experimental study can also be used for detailed tests of RANS and LES models, which will be undertaken in future studies.

It would be of interest in future studies to establish how the turbulence response depends on possible variations to the straining history, the Reynolds number, and the level of initial isotropy.

Appendix A. Application of rapid distortion theory

The evolution of one-dimensional energy spectra can be obtained by integrating the three-dimensional spectra according to

$$E_{11}(\kappa_1, t) = \int_{-\infty}^{\infty} \int_{-\infty}^{\infty} E_{11}^r(\boldsymbol{\kappa}, t)\, \mathrm{d}\kappa_2\, \mathrm{d}\kappa_3. \tag{A 1}$$

E_{11}^r is given by RDT prediction (Batchelor & Proudman 1954; Lee, Piomelli & Reynolds 1986):

$$E_{11}^r(\boldsymbol{\kappa}, t) = \frac{E(\kappa, 0)}{4\pi\kappa^2} \frac{1}{\chi^4} \left[(e_3^2/e_2^2)\kappa_2^2(\kappa_1^2 + \kappa_2^2) + (e_2^2/e_3^2)\kappa_3^2(\kappa_3^2 + \kappa_1^2) + 2\kappa_2^2\kappa_3^2 \right], \tag{A 2}$$

where $e_1(t) = 1/e_2(t) = e(t) = \exp(\int_{t_0}^{t} S(t) \, dt)$ and $e_3(t) = 1$ for planar straining, and $\chi^2 = \kappa_1^2/e_1^2 + \kappa_2^2/e_2^2 + \kappa_3^2/e_3^2$. $E(\kappa, 0)$ is the initial spectrum taken here as (Pope 2000)

$$E(\kappa, 0) = C_\kappa \varepsilon_0^{2/3} \kappa^{-5/3} f_L(\kappa l_0) f_\eta(\kappa \eta_0) \tag{A 3}$$

with

$$f_L(\kappa l_0) = \left(\frac{\kappa l_0}{[(\kappa l_0)^2 + 6.78]^{1/2}} \right)^{11/3} \tag{A 4}$$

and

$$f_\eta(\kappa \eta_0) = \exp \left(-5.2 \left\{ [(\kappa \eta_0)^4 + 16]^{1/4} - 2.0 \right\} \right). \tag{A 5}$$

The integral scale, l_0, and Kolmogorov scale, η_0, are given in table 1. The variance can be evaluated in spherical coordinates with x_3 as the axial direction according to

$$\langle u_1' u_1' \rangle(t) = \int_0^\infty \left(\int_0^\pi \left(\int_0^{2\pi} E_{11}^r(\kappa, t) \, d\theta \right) \sin \varphi \, d\varphi \right) \kappa^2 \, d\kappa. \tag{A 6}$$

Then, the normalized Reynolds stress r_{ij} is obtained by integrating (A 6) over θ and φ, i.e.

$$
\begin{aligned}
r_{11} &= \frac{\langle u_1' u_1' \rangle}{\langle u_1' u_1' \rangle_{t_0}} \\
&= \frac{3}{8\pi} \int_0^\pi \int_0^{2\pi} \frac{e^2 \sin^2 \theta \sin^4 \varphi + \frac{1}{e^2} \cos^2 \varphi (\cos^2 \varphi + \sin^2 \varphi \cos^2 \theta) + 2 \sin^2 \theta \sin^2 \varphi \cos^2 \varphi}{\left(\frac{1}{e^2} \sin^2 \theta \cos^2 \varphi + e^2 \sin^2 \theta \sin^2 \varphi + \cos^2 \varphi \right)^2} \\
&\quad \times d\theta \sin \varphi \, d\varphi
\end{aligned} \tag{A 7}
$$

All two-dimensional intergations are performed using the 'dblquad' routine in Mathlab®.

REFERENCES

BATCHELOR, G. K. & PROUDMAN, I. 1954 The effects of rapid distortion of a fluid in turbulent motion. *Q. J. Mech. Appl. Maths* **7**, 83–103.

CHEN, J., KATZ, J. & MENEVEAU, C. 2005 The implication of mismatch between stress and strain-rate in turbulence subjected to rapid straining and destraining on dynamic LES models. *Trans. ASME* I: *J. Fluids Engng* **127**, 840–850.

CHOI, K.-S. & LUMLEY, J. L. 2001 The return to isotropy of homogeneous turbulence. *J. Fluid Mech.* **436**, 59–84.

DORON, P., BERTUCCIOLI, L., KATZ, J. & OSBORN, T. 2001 Turbulence characteristics and dissipation estimates in the costal ocean bottom boundary layer from PIV data. *J. Phys. Oceanogr* **31**, 2108–2134.

EGGLES, J., UNGER, F., WEISS, M. H. *et al.* 1994 Fully developed turbulent pipe flow: a comparison between direct numerical simulation and experiment. *J. Fluid Mech.* **268**, 175–209.

ELSNER, J. & ELSNER, W. 1996 On the measurement of turbulence energy dissipation. *Meas. Sci. Technol.* **7**, 1334–1346.

FOUCAUT, J. & STANISLAS, M. 2002 Some considerations on the accuracy and frequency response of some derivative filters applied to particle image velocimetry vector fields. *Meas. Sci. Technol.* **13**, 1058–1071.

FRIEDMAN, P. & KATZ, J. 2002 Mean rise rate of droplets in isotropic turbulence. *Phys. Fluids* **14**, 3059–3073.

GENCE, J. N. & MATHIEU, J. 1979 On the application of successive plane strains to grid-generated turbulence. *J. Fluid Mech.* **93**, 501–513.

GENCE, J. N. & MATHIEU, J. 1980 The return to isotropy of a homogeneous turbulence having been submitted to two successive plane strains. *J. Fluid Mech.* **101**, 555–566.

HADZIC, I., HANJALIC, K. & LAURENCE, D. 2001 Modeling the response of turbulence subjected to cyclic irrotational strain. *Phys. Fluids* **13**, 1739–1747.

HINZE, J. O. 1987 *Turbulence*. McGraw–Hill.

HUANG, H., DIABIRI, D. & GHARIB, M. 1997 On the error of digital particle image velocimetry. *Meas. Sci. Technol.* **8**, 1427–1440.

HUNT, J. & CARRUTHERS, D. 1990 Rapid distortion theory and the problems of turbulence. *J. Fluid Mech.* **212**, 497–532.

HWANG, W. & EATON, J. K. 2004 Creating homogeneous and isotropic turbulence without a mean flow. *Phys. Fluids* **36**, 444–454.

KANG, H., CHESTER, S. & MENEVEAU, C. 2003 Decaying turbulence in an active-grid-generated flow and comparisons with large-eddy simulation. *J. Fluid Mech.* **480**, 129–160.

KEANE, R. & ADRIAN, R. 1990 Optimization of particle image velocimeters. Part I. Double pulsed systems. *Meas. Sci. Technol.* **1**, 1202–1215.

KEFFER, J. 1965 The uniform distortion of a turbulent wake. *J. Fluid Mech.* **22**, 135–159.

KEVLAHAN, N. & HUNT, J. 1997 Nonlinear interactions in turbulence with strong irrotational straining. *J. Fluid Mech.* **337**, 333–364.

KOPP, G., KAWALL, J. & KEFFER, J. 1995 The evolution of the coherent structures in a uniformly distorted plane turbulent wake. *J. Fluid Mech.* **291**, 299–322.

LEE, M. & REYNOLDS, W. 1985 Numerical experiments on the structure of homogeneous turbulence. *Stanford University Rep.* TF-24.

LEE, M., PIOMELLI, U. & REYNOLDS, W. 1986 Useful formulas in the rapid distortion theory of homogeneous turbulence. *Phys. Fluids* **29**, 3471–3474.

LIU, S., MENEVEAU, C. & KATZ, J. 1994 On the properties of similarity subgrid-scale models as deduced from measurement in turbulent jet. *J. Fluid Mech.* **275**, 83–119.

LIU, S., KATZ, J., & MENEVEAU, C. 1999 Evolution and modelling of subgrid scales during rapid straining of turbulence. *J. Fluid Mech.* **387**, 281–320.

MAKITA, H. 1991 Realization of a large-scale turbulence field in a small wind tunnel. *Fluid Dyn. Res.* **8**, 53–64.

MENEVEAU, C. & KATZ, J. 2000 Scale-invariance and turbulence models for large-eddy simulation. *Annu. Rev. Fluid Mech* **32**, 1–32.

MONIN, A. & YAGLOM, A. 1971 *Statistical Fluid Mechanics*. MIT Press.

MYDLARSKI, L. & WARHAFT, Z. 1996 On the onset of high-Reynolds-number grid-generated wind tunnel turbulence. *J. Fluid Mech.* **320**, 331–368.

MYDLARSKI, L. & WARHAFT, Z. 1998 Passive scalar statistics in high-Péclet-number grid turbulence. *J. Fluid Mech.* **358**, 135–175.

PIOMELLI, U., CABOT, W., MOIN, P. & LEE, S. 1991 Subgrid-scale backscatter in turbulent and transitional flows. *Phys. Fluids* A **3**, 1766–1771.

PIOMELLI, U., COLEMAN, G. & KIM, J. 1997 On the effects of nonequilibrium on the subgrid-scale stresses. *Phys. Fluids* **9**, 2740–2748.

POPE, S. 2000 *Turbulent Flows*. Cambridge University Press.

PRANDTL, L. 1933 Attaining a steady air stream in wind tunnels. *NACA TM* **726**.

RAFFEL, M., WILLERT, C. & KOMPENHANS, J. 1998 *Particle Image Velocimetry – A Practical Guide*. Springer.

REYNOLDS, A. 1962 Observations on distorted turbulent wakes. *J. Fluid Mech.* **13**, 333–355.

REYNOLDS, W. 1990 The potential and limitation of direct and large eddy simulations. In (*Whither Turbulence? Or Turbulence at Crossroads.* In J. L. Lumley ed.) Springer.

ROGALLO, R. & MOIN, P. 1984 Numerical simulation of turbulent flows. *Annu. Rev. Fluid Mech.* **16**, 99–137.

ROTH, G. & KATZ, J. 2001 Five techniques for increasing the speed and accuracy of PIV interrogation. *Meas. Sci. Technol.* **12**, 238–245.

ROTH, G., MASCENIK, D. & KATZ, J. 1999 Measurements of the flow structure and turbulence within a ship bow wave. *Phys. Fluids* **11**, 3512–3523.

SADDOUGHI, S. & VEERAVALLI, S. V. 1994 Local isotropy in turbulent boundary layers at high Reynolds number. *J. Fluid Mech.* **268**, 333–372.

SAVILL, A. M. 1987 Recent developments in rapid-distortion theory. *Annu. Rev. Fluid Mech.* **19**, 531–575.

TAYLOR, G. 1935 Turbulence in a contracting stream. *Z. Angew. Math. Mech* **15**, 91–96.

TEIXEIRA, M. & BELCHER, S. 2002 On the distortion of turbulence by a progressive surface wave. *J. Fluid Mech.* **458**, 229–267.

TENNEKES, H. & LUMLEY, J. 1972 *A First Course in Turbulence*. MIT Press.

TOWNSEND, A. 1954 The uniform distortion of homogeneous turbulence. *Q. J. Mech. Appl. Maths* **7**, 104–127.

TUCKER, H. & REYNOLDS, A. 1968 The distortion of turbulence by irrotational plane strain. *J. Fluid Mech.* **32**, 657–673.